Jianxun Wang
Department of Electrical and Computer Engineering,
Michigan State University,
East Lansing, MI 48824
e-mail: wangji19@msu.edu

Philip K. McKinley
Department of Computer Science and Engineering,
Michigan State University,
East Lansing, MI 48824
e-mail: mckinley@cse.msu.edu

Xiaobo Tan[1]
Department of Electrical and Computer Engineering,
Michigan State University,
East Lansing, MI 48824
e-mail: xbtan@msu.edu

Dynamic Modeling of Robotic Fish With a Base-Actuated Flexible Tail

In this paper, we develop a new dynamic model for a robotic fish propelled by a flexible tail actuated at the base. The tail is modeled by multiple rigid segments connected in series through rotational springs and dampers, and the hydrodynamic force on each segment is evaluated using Lighthill's large-amplitude elongated-body theory. For comparison, we also construct a model using linear beam theory to capture the beam dynamics. To assess the accuracy of the models, we conducted experiments with a free-swimming robotic fish. The results show that the two models have almost identical predictions when the tail undergoes small deformation, but only the proposed multisegment model matches the experimental measurement closely for all tail motions, demonstrating its promise in the optimization and control of tail-actuated robotic fish. [DOI: 10.1115/1.4028056]

1 Introduction

Biomimetic systems have been receiving increasing attention from the robotics community, since natural organisms can provide important insights into the theory and design of engineer systems. For example, in the area of aquatic robots, the maneuverability and efficiency of live fish [1,2] have motivated significant scientific interest over the past two decades in developing, modeling, and controlling robotic fish [3–17]. In addition to providing platforms for underwater applications such as environmental monitoring [18–20], these robots offer a means to study the behavior of live fish [21].

Numerous designs of actuation mechanisms have been proposed for robotic fish [3,9,10,17,21–33]. A typical approach is to use multiple links actuated separately or jointly to deform the body itself [3,6,14,17,34,35], which requires multiple actuators and/or complex transmission mechanisms. Another class of designs involves an oscillating caudal fin (e.g., [4,9,10,30,36]), sometimes in conjunction with pectoral fins [9]. Among various designs, tail actuation is especially attractive since it is easy to realize, enables both forward swimming and turning maneuvers, and leaves the majority of the body free of moving parts. The latter is important when the robot is used in applications such as mobile sensing, where the body space can be maximally used to house sensors and electronics [20]. Many tail-actuation designs involve rigid, oscillating plates [9,12,13,37]. This design lends itself to simple construction and tractable analysis. However, it has been recognized that the flexibility of body and fin structures has a pronounced impact on the swimming performance of biological and robotic fish [16,38,39]. Flexible caudal fins can be realized by motor-driven compliant beams or plates [17,36,40], or directly through soft actuation materials such as ionic polymer–metal composites (IPMCs) [4,7,10,30]. While these active materials possess intriguing properties, the thrust they can produce is still relatively weak and the long-term repeatability of their actuation behavior is yet to be established. Therefore, base-actuated soft, passive structures remain a competitive option for flexible tails.

To design and control robotic fish actuated with a flexible tail, it is essential to have a faithful and efficient dynamic model. Modeling of a flexible beam attached to a moving base in the air has been studied by a number of researchers [,40–43]. However, in this work, a major challenge in the modeling lies in properly capturing the fluid–structure interactions and the resulting force and moment on the robot. Most existing work on modeling has dealt with rigid fins [9,12,13,37,44,45], although modeling of flexible fins has been conducted recently by several groups [10,17,30,46]. In Ref. [17], Alvarado and Youcef Toumi focused on designing compliant bodies to achieve biomimetic locomotion efficiency and maneuverability. To demonstrate the results, they also compared the experimental results with the linear beam model. Researchers have also developed models that capture the actuation physics of an anchored IPMC beam and the complex hydrodynamic interactions between IPMC and fluid [10,30]. In Ref. [46], Kopman and Porfiri described a modular biomimetic robotic fish developed for educational activities, along with a modeling framework for predicting the robot's static thrust production. In all these studies, a linear Euler–Bernoulli beam model was adopted to describe the beam dynamics. A disadvantage of this approach is that, under large oscillations, these models do not accurately capture the beam dynamics [47–49] and consequently the hydrodynamics.

In this work, we take a significant departure from the beam model approach by approximating a flexible tail with multiple rigid segments connected in series through torsional springs and dampers. A similar multisegment approach has been used to model a beam under large deformation in air [49,50] and model a flexible beam in flow sensing [51]. However, the multisegment beam model has not been explored in the modeling of a base-actuated flexible beam subject to complex hydrodynamic interactions. For comparison, we also present a model based on linear beam theory, as widely adopted in other studies [10,17,30,46]. Note that, for ease of presentation, a tail with uniform height is considered in this work. Despite its simple appearance, this case captures the key essential challenges (nonlinear beam dynamics under large deformation, coupled with hydrodynamic interactions) that would be present for cases with more general tail shapes. We evaluate the hydrodynamic force on the actuating tail using Lighthill's large-amplitude elongated-body theory [52], because it has a sound balance between fidelity and simplicity and its effectiveness in robotic fish modeling has been demonstrated in our prior work [13,30]. A weakness of Lighthill's theory is that it neglects the

[1]Corresponding author.

Contributed by the Dynamic Systems Division of ASME for publication in the Journal of Dynamic Systems, Measurement, and Control. Manuscript received July 8, 2013; final manuscript received July 17, 2014; published online August 28, 2014. Assoc. Editor: Evangelos Papadopoulos.

effect of vortex wake on the pressure distribution on the body and thus neglects the effect of vortex shedding on the thrust production [53]. Incorporating such vortex-shedding effects (for example, using the vortex ring panel method [54]), however, typically requires computational fluid dynamics (CFD) simulation and is not amenable to the development of a model that is suitable for robot optimization and control, which is the goal of this paper.

To compare and validate the models, we conduct extensive experiments with a robotic fish prototype. We find that both models have similar predictions that are close to the experimental measurements when the flexible beam is under small deformations. However, the discrepancy between the predictions becomes greater as the beam experiences larger deformations. In particular, we show that the multisegment model is able to predict precisely the transient trajectory and steady-state speed of the free-swimming robot, as well as the dynamic shape of the tail, under a wide range of actuation inputs. In comparison, the linear beam model-based approach is only able to capture the robot speed and tail shape when the tail undergoes relatively small deformations. A preliminary version of this paper was presented at the 2012 ASME Dynamic Systems and Control Conference [55].

The remainder of the paper is organized as follows. The overall dynamic model for a tail-actuated robotic fish is first reviewed in Sec. 2, where the hydrodynamic forces generated by the tail are evaluated by Lighthill's theory. The use of Lighthill's theory requires knowing the tail shape as a function of time, which is the main focus of this paper. The Euler–Bernoulli beam-based model and the multisegment model for the based-actuated flexible tail are developed in Secs. 3 and 4, respectively. Experimental validation and comparison of the models are presented in Sec. 5. Finally, concluding remarks are provided in Sec. 6.

2 The Overall Dynamic Model for Tail-Actuated Robotic Fish

The robot is assumed to comprise two parts, a rigid body and a flexible tail. The motion of the robot body is governed by rigid-body dynamics with the added-mass effect incorporated. Lighthill's large-amplitude elongated-body theory is adopted to evaluate the hydrodynamic forces generated by the flexible tail's motion. We assume that the height of the tail does not vary abruptly along its length, thus meeting the "elongated body" requirement [52].

2.1 Rigid-Body Dynamics. Figure 1 shows a schemata of the robotic fish, with $[X,Y,Z]$ denoting the inertial coordinates, and $[x,y,z]$ denoting the body-fixed coordinates with unit vectors $[\hat{x},\hat{y},\hat{z}]$. We denote by $\hat{m}$ and $\hat{n}$ the unit vectors parallel and perpendicular to the tail, respectively. We assume that both the body and the tail are neutrally buoyant, and that the center of gravity of the body coincides with the center of geometry at point C. The velocity at C expressed in the body-fixed coordinates $\mathbf{V}_C = [V_{Cx}, V_{Cy}, V_{Cz}]^{\mathrm{T}}$ comprises surge (V_{Cx}), sway (V_{Cy}), and heave (V_{Cz}) components. In addition, the angular velocity $\boldsymbol{\omega} = [\omega_x, \omega_y, \omega_z]^{\mathrm{T}}$ comprises roll (ω_x), pitch (ω_y), and yaw (ω_z) expressed in the body-fixed coordinates. We use α to denote the tail deflection angle (the tangential direction of the flexible tail at the base) with respect to the negative x–axis, and β to denote the angle of attack, formed by the direction of $\mathbf{V}_C$ with respect to the x–axis. Finally, ψ denotes the heading angle, formed by the x–axis relative to the X–axis.

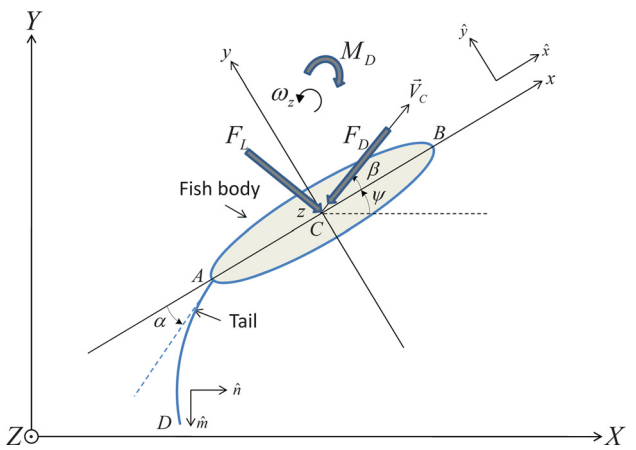

Fig. 1 Schematic representation of the robotic fish in planar motion

The linear momentum $\mathbf{P}$ and angular momentum $\mathbf{H}$ of the body in the body-fixed coordinates are expressed as

$$\mathbf{P} = \mathbf{M}\cdot\mathbf{V}_C + \mathbf{D}^T\cdot\boldsymbol{\omega} \tag{1}$$

$$\mathbf{H} = \mathbf{D}\cdot\mathbf{V}_C + \mathbf{J}\cdot\boldsymbol{\omega} \tag{2}$$

where $\mathbf{M}$ and $\mathbf{J}$ are the mass and inertia matrices, respectively, and $\mathbf{D}$ is the Coriolis and centripetal matrix. For a rigid body in an inviscid fluid, Kirchhoff's equations of motion in the body-fixed frame are [56,57]

$$\dot{\mathbf{P}} = \mathbf{P}\times\boldsymbol{\omega} + \mathbf{F} \tag{3}$$

$$\dot{\mathbf{H}} = \mathbf{H}\times\boldsymbol{\omega} + \mathbf{P}\times\mathbf{V}_C + \mathbf{M} \tag{4}$$

where $\mathbf{F} = [F_x, F_y, F_z]^{\mathrm{T}}, \mathbf{M} = [M_x, M_y, M_z]^{\mathrm{T}}$ denote the external forces and moments about the body center C, respectively, and "$\times$" denotes the vector product. The assumption of neutral buoyancy implies that these forces and moments will only come from the hydrodynamic interactions between the robot (including both the body and the tail) and the fluid. As to be explained in more detail, these interactions include hydrodynamic forces/moments due to the tail motion, which are evaluated with Lighthill's theory (Sec. 2.2), and the lift and drag on the robot body itself (Sec. 2.3).

We further assume that the body is symmetric with respect to the xz–plane and the tail moves in the xy–plane. Consequently, the heave velocity V_{Cz}, the roll rate ω_z, and the pitch rate ω_y are all equal to zero, in which case the system has three degrees of freedom, namely, surge (V_{Cx}), sway (V_{Cy}), and yaw (ω_z). We further assume that the inertial coupling between the surge, sway, and yaw motions is negligible [10], implying $\mathbf{D}=0$. Under these assumptions and following Ref. [56], Eqs. (3) and (4) can be simplified as

$$(m_{\mathrm{b}} - X_{\dot{V}_{Cx}})\dot{V}_{Cx} = (m_{\mathrm{b}} - Y_{\dot{V}_{Cy}})V_{Cy}\omega_z + F_x \tag{5}$$

$$(m_{\mathrm{b}} - Y_{\dot{V}_{Cy}})\dot{V}_{Cy} = -(m_{\mathrm{b}} - X_{\dot{V}_{Cx}})V_{Cx}\omega_z + F_y \tag{6}$$

$$(J_{\mathrm{b}z} - N_{\dot{\omega}_z})\dot{\omega}_z = (Y_{\dot{V}_{Cy}} - X_{\dot{V}_{Cx}})V_{Cx}V_{Cy} + M_z \tag{7}$$

where m_{b} is the mass of the body and $J_{\mathrm{b}z}$ is the inertia of the body about the z–axis. $X_{\dot{V}_{Cx}}, Y_{\dot{V}_{Cy}}$, and $N_{\dot{\omega}_z}$ are the hydrodynamic derivatives that represent the effect of added mass on the body. Finally, the kinematic equations for the robot are

$$\dot{X} = V_{Cx}\cos\psi - V_{Cy}\sin\psi \tag{8}$$

$$\dot{Y} = V_{Cy}\cos\psi + V_{Cx}\sin\psi \tag{9}$$

$$\dot{\psi} = \omega_z \tag{10}$$

2.2 Lighthill's Large-Amplitude Elongated-Body Theory. Lighthill's theory was originally developed to describe the hydrodynamic force experienced by a fish swimming in a horizontal plane. In this paper, we apply this theory to the base-actuated flexible tail of a robotic fish. As illustrated in Fig. 2, the tail is assumed to be inextensible and is parameterized by τ, with $\tau=0$

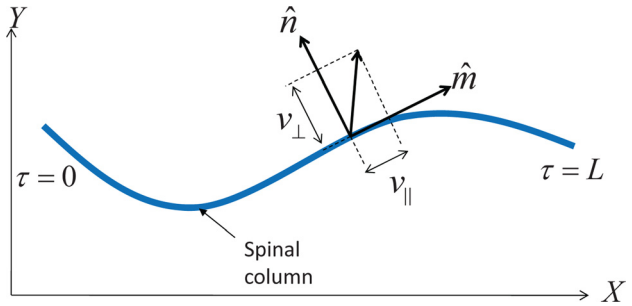

Fig. 2 Illustration of the coordinate system for flexible tail (top view)

denoting the anterior end and $\tau = L$ denoting the posterior end. The coordinates $(X(\tau,t), Y(\tau,t))$, $0 \le \tau \le L$, denote the trajectory of each point τ on the tail at time t, which could be due to tail dynamics or the resulting translational/rotational motion of the whole fish. A frame of reference is chosen such that the water far from the robotic fish is at rest.

Following Ref. [52], given $(X(\tau,t), Y(\tau,t))$, the hydrodynamic reactive force density due to the added-mass effect at each point $\tau < L$ is

$$\mathbf{f}(\tau) = \begin{pmatrix} f_X(\tau) \\ f_Y(\tau) \end{pmatrix} = -m_{\mathrm{w}} \frac{\mathrm{d}}{\mathrm{d}t}(v_\perp \hat{n}) \tag{11}$$

and at $\tau = L$, there is a concentrated force

$$\mathbf{F}_C = \begin{pmatrix} F_{CX} \\ F_{CY} \end{pmatrix} = \left[-\frac{1}{2} m_{\mathrm{w}} v_\perp^2 \hat{m} + m_{\mathrm{w}} v_\perp v_\parallel \hat{n} \right]_{\tau=L} \tag{12}$$

In Eqs. (11) and (12), m_{w} denotes the virtual mass per unit length and it can be approximated by $\frac{1}{4}\pi\rho_{\mathrm{w}} d^2$, where ρ_{w} is the density of water and d is the depth of tail cross section (in Z direction) at τ (and thus can vary with τ). The two terms in Eq. (12) account for the pressure force acting on Π and the force due to convection of momentum out of $\mathscr{V}$ across Π, respectively, where Π is the plane at $\tau = L$ that is perpendicular to $\hat{m}$, and $\mathscr{V}$ is the half-space bounded by Π that includes the tail but excludes the wake [52]. As illustrated in Fig. 2, $\hat{m} = (\partial X/\partial\tau, \partial Y/\partial\tau)^T$ and $\hat{n} = (-\partial Y/\partial\tau, \partial X/\partial\tau)^T$ represent the unit vectors tangential and perpendicular to the spinal column, respectively, and $v_\parallel$ and $v_\perp$ represent the components of the velocity $\mathbf{v} = (\partial X/\partial t, \partial Y/\partial t)^T$ at τ in $\hat{m}$ and $\hat{n}$ directions, respectively,

$$v_\parallel = \langle \mathbf{v}, \hat{m} \rangle = \frac{\partial X}{\partial t}\frac{\partial X}{\partial \tau} + \frac{\partial Y}{\partial t}\frac{\partial Y}{\partial \tau} \tag{13}$$

$$v_\perp = \langle \mathbf{v}, \hat{n} \rangle = -\frac{\partial X}{\partial t}\frac{\partial Y}{\partial \tau} + \frac{\partial Y}{\partial t}\frac{\partial X}{\partial \tau} \tag{14}$$

where $\langle \cdot, \cdot \rangle$ denotes the inner product of vectors. We note that the actual mass of the tail is negligible (relative to the virtual mass) when the width of the tail is much thinner than the height [52], which is typically true for the tail of a robotic fish. For example, in the model validation part of this work, we use a flexible tail with a height of 2.5 cm and a thickness of 0.3 mm, which indicates that m_{w} is 490.9 g/m. In contrast, the physical tail, which has a length of 8 cm, weighs 0.54 g, resulting in a mass of 6.75 g/m, which is 1.38% of the virtual mass. Hydrodynamic moments experienced by the robot body that are due to the tail can be evaluated accordingly based on $\mathbf{f}(\tau)$ and $\mathbf{F}_C$.

2.3 Drag and Lift on the Body. As shown in Fig. 1, besides the hydrodynamic force and moment transmitted from the tail, the robot body also experiences drag force F_{D}, lift force F_{L}, and drag moment M_{D} [9,10,37], which can be represented as

$$F_{\mathrm{D}} = \frac{1}{2}\rho |V_C|^2 S C_{\mathrm{D}} \tag{15}$$

$$F_{\mathrm{L}} = \frac{1}{2}\rho |V_C|^2 S C_{\mathrm{L}} \beta \tag{16}$$

$$M_{\mathrm{D}} = -C_M \omega_z^2 \mathrm{sgn}(\omega_z) \tag{17}$$

where S is a suitably defined reference surface area for the robot body, and C_{D}, C_{L}, and C_{M} are the drag force coefficient, lift coefficient, and drag moment coefficient, respectively.

Finally, by adding the hydrodynamic forces and moments from the tail and those directly on the body, we obtain F_x, F_y, and M_z in Eqs. (5)–(7) as

$$F_x = F_{hx} - F_{\mathrm{D}} \cos\beta + F_{\mathrm{L}} \sin\beta \tag{18}$$

$$F_y = F_{hy} - F_{\mathrm{D}} \sin\beta - F_{\mathrm{L}} \cos\beta \tag{19}$$

$$M_z = M_{hz} + M_{\mathrm{D}} \tag{20}$$

where F_{hx}, F_{hy}, and M_{hz} are the projections of hydrodynamic forces caused by tail motion, and the resulting moment relative to the center C of the robot body.

3 Dynamic Modeling of a Tail Using Euler–Bernoulli Beam Theory

The application of Lighthill's theory requires knowing the shape trajectory of the base-actuated flexible tail. We propose a multisegment approach to the modeling of the tail that undergoes large deformations in Sec. 4. But in this section we first develop a comparative approach based on linear beam theory, which has been widely used in the relevant literature. We focus on beam modeling with the robot anchored, as typically adopted in the literature [17,46]. Figure 3 illustrates this approach; the dashed line represents a rotating frame, which coincides with the line tangential to the tail at the base, and the blue solid curve represents the shape of the flexible caudal fin. The transverse displacement of points on the flexible tail relative to the rotating base, due to the beam's vibration, is given by $w(\tau,t)$. We note that the tail is assumed to be under small deformation in accordance with the Euler–Bernoulli theory. In other words, the motion direction of each point along the flexible tail is perpendicular to the dashed line.

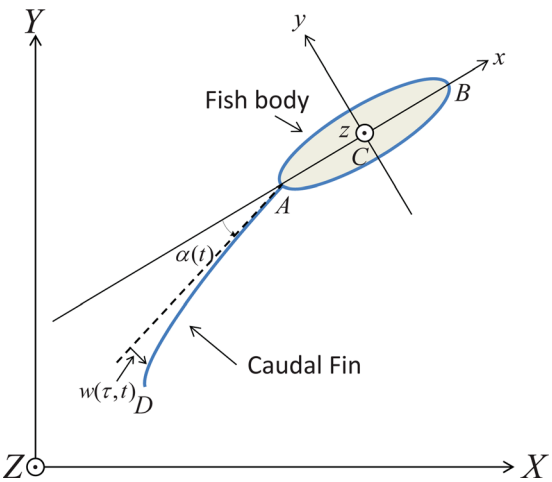

Fig. 3 Passive flexible tail modeled by Euler–Bernoulli linear beam approach

The tail is excited by the oscillating support at the point A, with

$$\left[\frac{\partial w_1(\tau,t)}{\partial \tau}\right]_{\tau=0} = \left[\frac{\partial w_2(\tau,t)}{\partial \tau}\right]_{\tau=0} = \alpha(t) \tag{21}$$

Here $w_1(\tau,t)$ denotes the beam displacement in the inertial frame and $w_2(\tau,t)$ accounts for the rigid-body (rotating base) motion

$$\begin{aligned} w_1(\tau,t) &= w_2(\tau,t) + w(\tau,t) \\ w_2(\tau,t) &= \tau \cdot \alpha(t) \end{aligned} \tag{22}$$

The forced underwater vibration of the flexible beam is described by the following equation [46,58]:

$$\frac{\partial^2}{\partial \tau^2}\left[EI(\tau)\frac{\partial^2 w_1(\tau,t)}{\partial \tau^2}\right] + m(\tau)\frac{\partial^2 w_1(\tau,t)}{\partial t^2} = p(\tau,t) \tag{23}$$

where E denotes the Young's modulus of the flexible tail, I denotes the area moment of inertia, $m(\tau)$ denotes the mass of the tail per unit length, and $p(\tau,t)$ denotes the transverse loading on the tail which is caused by the interactions between the tail and the surrounding aquatic environment that can be evaluated by Lighthill's theory. Unlike Refs. [17] and [46], in this work we also consider distributed viscous damping introduced by the internal resistance opposing the strain velocity [58], which leads to

$$\frac{\partial^2}{\partial \tau^2}\left[EI(\tau)\left(\frac{\partial^2 w_1(\tau,t)}{\partial \tau^2} + \kappa\frac{\partial^3 w_1(\tau,t)}{\partial \tau^2 \partial t}\right)\right] + m(\tau)\frac{\partial^2 w_1(\tau,t)}{\partial t^2} = p(\tau,t) \tag{24}$$

where κ is the stiffness proportionality factor for Rayleigh damping.

Similar to Refs. [12] and [13], we assume that the tail itself has negligible mass compared to the added mass effects. Then following Lighthill's theory, we obtain

$$EI\left[\frac{\partial^4 w(\tau,t)}{\partial \tau^4} + \kappa\frac{\partial^5 w(\tau,t)}{\partial \tau^4 \partial t}\right] + m_{\mathrm{w}}\frac{\partial^2 w(\tau,t)}{\partial t^2} = P_{\mathrm{eff}}(\tau,t) \tag{25}$$

in which

$$P_{\mathrm{eff}}(\tau,t) = -EI\left[\frac{\partial^4 w_2(\tau,t)}{\partial \tau^4} + \kappa\frac{\partial^5 w_2(\tau,t)}{\partial \tau^4 \partial t}\right] - m_{\mathrm{w}}\frac{\partial^2 w_2(\tau,t)}{\partial t^2}$$

represents the effective distributed dynamic loading caused by the prescribed support excitations, and m_{w} is virtual mass per unit length defined previously, accounting for the added mass effect. Since the first two terms of $P_{\mathrm{eff}}(\tau,t)$ are equal to zero as $w_2(\tau,t) = \tau \cdot \alpha(t)$, the tail beam can be modeled as

$$EI\left[\frac{\partial^4 w(\tau,t)}{\partial \tau^4} + \kappa\frac{\partial^5 w(\tau,t)}{\partial \tau^4 \partial t}\right] + m_{\mathrm{w}}\frac{\partial^2 w(\tau,t)}{\partial t^2} = -m_{\mathrm{w}}\tau \cdot \ddot{\alpha}(t) \tag{26}$$

Using the modal analysis method, we can express the solution of Eq. (26) as the sum of an infinite number of modes

$$w(\tau,t) = \sum_{i=1}^{\infty} \phi_i(\tau)\eta_i(t) \tag{27}$$

where $\phi_i(\tau)$ is the beam shape for the ith mode and $\eta_i(t)$ is the corresponding generalized coordinate. There is no concentrated force in the $\hat{n}$ direction with the anchored body assumption, which implies that the boundary conditions for $w(\tau,t)$ is the same as those for a cantilever beam

$$\begin{aligned} w(0,t) = 0, \quad \frac{\partial w}{\partial \tau}(0,t) = 0 \\ EI\frac{\partial^2 w}{\partial \tau^2}(L,t) = 0, \quad EI\frac{\partial^3 w}{\partial \tau^3}(L,t) = 0 \end{aligned} \tag{28}$$

The mode shape $\phi_i(\tau)$ takes the form

$$\phi_i(\tau) = (\cos\beta_i\tau - \cosh\beta_i\tau) - \delta_i(\sin\beta_i\tau - \sinh\beta_i\tau) \tag{29}$$

where β_i can be obtained by solving

$$1 + \cos\beta_i L \cosh\beta_i L = 0$$

and

$$\delta_i = \frac{\cos\beta_i L + \cosh\beta_i L}{\sin\beta_i L + \sinh\beta_i L}$$

With the damping ratio for the ith mode

$$\xi_i = \frac{\kappa\omega_i}{2}$$

where ω_i is the natural frequency for the ith mode,

$$\omega_i = \beta_i^2\sqrt{\frac{EI}{m_{\mathrm{w}}}} \tag{30}$$

$\eta_i(t)$ can be solved from

$$\frac{\mathrm{d}^2\eta_i(t)}{\mathrm{d}t^2} + 2\xi_i\omega_i\frac{\mathrm{d}\eta_i(t)}{\mathrm{d}t} + \omega_i^2\eta_i(t) = \frac{Q_i(t)}{M_i}, \quad i = 1,2\ldots \tag{31}$$

where

$$Q_i(t) = \int_0^L \phi_i(\tau)P_{\mathrm{eff}}(\tau,t)\mathrm{d}\tau \tag{32}$$

and

$$M_i = \int_0^L \phi_i(\tau)^2 m_{\mathrm{w}}\mathrm{d}\tau \tag{33}$$

When the tail shaft oscillates sinusoidally, we can obtain a closed-form solution for $\eta_i(t)$. Consider in particular the following form for the base angle:

$$\alpha(t) = \alpha_0 + \alpha_A\sin(\omega_\alpha t + \phi_\alpha) \tag{34}$$

where α_0, α_A, ω_α, and ϕ_α denote the bias, amplitude, frequency, and initial phase of the tail beat, respectively. Then, we have

$$\eta_i(t) = \frac{m_{\mathrm{w}}\alpha_A\omega_\alpha^2\int_0^L \tau\phi_i(\tau)\mathrm{d}\tau}{M_i Z_i \omega_\alpha}\sin(\omega_\alpha t + \phi_\alpha + \phi_i) \tag{35}$$

where

$$Z_i = \sqrt{(2\omega_i\xi_i)^2 + \frac{1}{\omega_\alpha^2}(\omega_\alpha^2 - \omega_i^2)^2}$$

is the magnitude of the impedance function and

$$\phi_i = \arctan\left(\frac{2\omega_\alpha\omega_i\xi_i}{\omega_\alpha^2 - \omega_i^2}\right)$$

is the phase lag of the oscillation relative to $\alpha(t)$. Using Eqs. (11) and (12), the total hydrodynamic force acting on the tail is then

$$\mathbf{F} = \int_0^L \mathbf{f}(\tau)d\tau - \left[\frac{1}{2}m_w v_\perp^2 \hat{m}\right]_{\tau=L} \tag{36}$$

where $\mathbf{f}(\tau) = -m_w[(\tau\ddot{\alpha} + (\partial^2 w/\partial t^2))\hat{n} - \dot{\alpha}(\tau\dot{\alpha} + (\partial w/\partial t))\hat{m}]$. The corresponding moment relative to the center C of the robot body is

$$\mathbf{M} = \int_0^L \mathbf{r}_{C\tau} \times \mathbf{f}(\tau)d\tau + \mathbf{r}_{CL} \times \left(-\left[\frac{1}{2}m_w v_\perp^2 \hat{m}\right]_{\tau=L}\right) \tag{37}$$

where $\mathbf{r}_{C\tau}$ and $\mathbf{r}_{CL}$ denote the vectors from the body center C to the point τ and L on the tail, respectively.

4 Dynamic Modeling of a Tail Using Multisegment Approximation

A fundamental underlying assumption in establishing the model described in Sec. 1 is that the flexible tail is under small deformation. However, based upon observation of the dynamic shape of the tail, this assumption does not always hold, especially when the tail undergoes large angular displacement and/or high-frequency oscillations. In this section, we propose a novel model by representing the tail as multiple rigid elements connected in series through torsional springs and dampers, to capture the large deformation of the beam. N rigid segments, with equal length of l, are used to represent the tail, as illustrated in Fig. 4. Each segment is linked with its neighboring segments through joints modeled by a torsional spring K_S and a viscous damper K_D.

Following Ref. [49], we can evaluate the stiffness of each torsional spring as:

$$K_S = \frac{Edh^3}{12l} \tag{38}$$

with h denoting the thickness of tail. K_D can be evaluated as $K_D = \kappa K_S$, where κ is the proportional constant as defined in the Sec. 1. Following Lighthill's large-amplitude elongated-body theory, we need to compute the motion of every point along the tail over time, in order to evaluate the tail actuation-induced hydrodynamic force. Consequently, we need to know the joint angles α_i, made by the ith link with respect to the negative x-axis (as illustrated in Fig. 4), so that Eqs. (11) and (12) can be applied to evaluate the hydrodynamic forces on the tail section. The displacement $\mathbf{r}_{\tau_i}$ of every point τ_i on the ith segment in the inertial frame can be described as

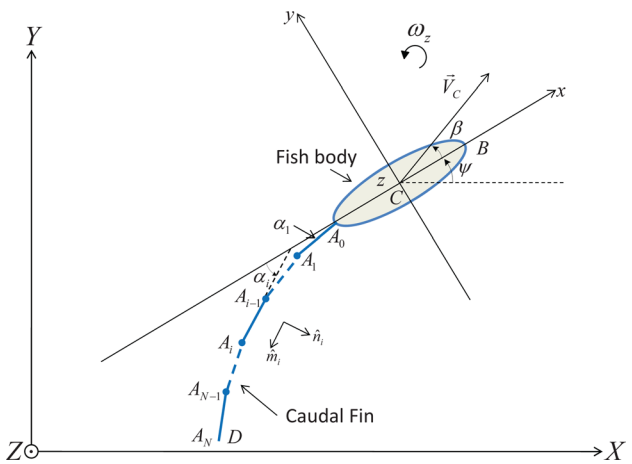

Fig. 4 Passive flexible tail modeled by multiple rigid segments

$$\mathbf{r}_{\tau_i} = l \cdot \left[\sum_{k=1}^{i-1} \hat{m}_k\right] + \tau_i \hat{m}_i \tag{39}$$

then the velocity perpendicular to the ith segment is

$$v_{\tau_i\perp} = l \cdot \left[\sum_{k=1}^{i-1} \dot{\alpha}_k \cos(\alpha_k - \alpha_i)\right] + \tau_i \dot{\alpha}_i \tag{40}$$

Therefore, the force density acting on the ith segment can be evaluated as

$$\begin{aligned}\mathbf{f}_{\tau_i} &= -m_w \frac{d}{dt}(v_{\tau_i\perp}\hat{n}_i) \\ &= -m_w\left\{l\sum_{k=1}^{i-1}[\ddot{\alpha}_k\cos(\alpha_i-\alpha_k) - \dot{\alpha}_k\sin(\alpha_i-\alpha_k)(\dot{\alpha}_i-\dot{\alpha}_k)] + \tau_i\ddot{\alpha}_i\right\}\hat{n}_i \\ &\quad + m_w\dot{\alpha}_i\left\{l\sum_{k=1}^{i-1}[\dot{\alpha}_k\cos(\alpha_i-\alpha_k)] + \dot{\alpha}_i\tau_i\right\}\hat{m}_i\end{aligned} \tag{41}$$

The total reactive force $\mathbf{F}_i$ on the ith segment, and the moment $\mathbf{M}_i$ relative to point A_{i-1} can be evaluated using

$$\mathbf{F}_i = \int^l \mathbf{f}_{\tau_i} d\tau, \quad \mathbf{M}_i = \int^l \tau_i \hat{m}_i \times \mathbf{f}_{\tau_i} d\tau \tag{42}$$

Defining $\mathbf{F}_{Ai}$ and $\mathbf{M}_{Ai}$ to be the force and the moment exerted by the $(i+1)$th segment on the ith segment, respectively, we can express the interactions between adjacent segments as

$$\mathbf{F}_{A_i} = \mathbf{F}_{i+1} + \mathbf{F}_{A_{i+1}} \tag{43}$$

$$\mathbf{M}_{A_i} = \mathbf{M}_{i+1} + \mathbf{M}_{A_{i+1}} + l\hat{m}_i \times \mathbf{F}_{A_{i+1}} \tag{44}$$

For the last segment of the tail, as illustrated in Fig. 4, the reactive force and moment are

$$\begin{aligned}\mathbf{F}_{A_N} &= -\frac{1}{2}m_w\left[l\sum_{k=1}^{N}\dot{\alpha}_k\cos(\alpha_N-\alpha_k)\right]^2\hat{m}_N \\ &\quad + m_w\left[l\sum_{k=1}^{N}\dot{\alpha}_k\cos(\alpha_N-\alpha_k)\right]\left[l\sum_{k=1}^{N}\dot{\alpha}_k\sin(\alpha_N-\alpha_k)\right]\hat{n}_N\end{aligned} \tag{45}$$

$$\mathbf{M}_{A_N} = 0 \tag{46}$$

Defining $\mathbf{M}_{(S+D)_i}$ the moment produced by the spring and damper at joint A_i, then the moment balance equation implies, for $i = 1, 2, \ldots, N-1$,

$$\mathbf{M}_{A_i} = \mathbf{M}_{(S+D)_i} \tag{47}$$

where

$$\mathbf{M}_{(S+D)_i} = [K_S(\alpha_{i+1} - \alpha_i) + K_D(\dot{\alpha}_{i+1} - \dot{\alpha}_i)]\hat{z} \tag{48}$$

Equation (47) has $(N-1)$ scalar equations involving $(N-1)$ unknown variables $\alpha_2, \cdots, \alpha_N$, which is solvable.

$\mathbf{F}_{A_0}$ is the force that the flexible tail exerts on the robotic fish body, which can be written as $\mathbf{F}_{A_0} = F_{hx}\cdot\hat{x} + F_{hy}\cdot\hat{y}$, where F_{hx} and F_{hy} are the components of F_A along $\hat{x}$ and $\hat{y}$, respectively. The moment to the center of the body caused by the oscillation of the tail can be evaluated as

$$\mathbf{M}_C = \mathbf{M}_{A_0} - c\hat{x} \times \mathbf{F}_{A_0} \tag{49}$$

It is clear that $\mathbf{M}_C$ is along the z direction, which we denote as M_{hz}.

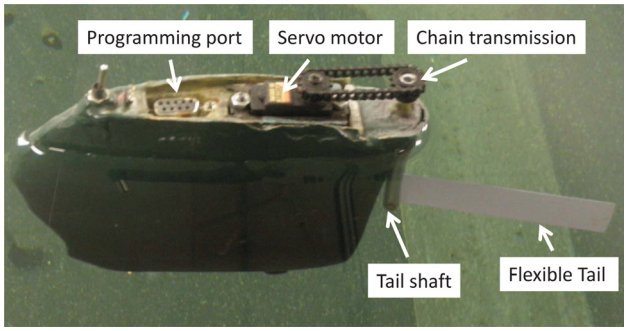

Fig. 5 A free-swimming robotic fish prototype used for model validation

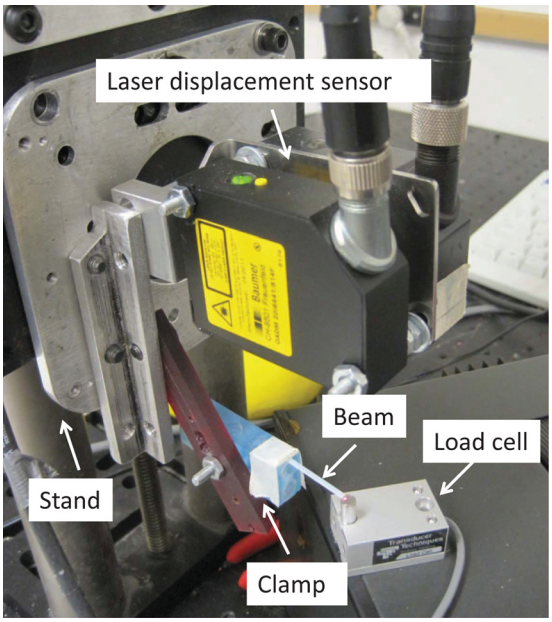

Fig. 6 Experimental setup for measuring the Young's modulus of the flexible tail

5 Experimental Model Validation

To evaluate the dynamic models described in Secs. 3 and 4, we have conducted experiments with the free-swimming robotic fish prototype shown in Fig. 5. The robot has a simple mechanism for actuation, and it satisfies most of the assumptions used in the modeling work, which facilitates model validation. In particular, the height of the tail does not change abruptly along the length direction, thus meeting the "elongated body" requirement. The thickness of the tail is much less than its height, so that the actual mass of the tail is much less than the virtual mass, as assumed in Sec. 2.2. Through a chain transmission mechanism, a servomotor (HS-5085MG from Hitec) is able to control the angular position of the tail shaft and thus the tail deflection angle α, i.e., sinusoidal motion, accurately. On the other hand, in the modeling work, we assume that the robot is anchored, as typically adopted in the literature. This assumption, of course, does not hold fully during free-swimming experiments, which might explain the slight discrepancies between the model predictions and experimental measurement in those experiments. The tail was a rectangular plastic slice, which was 8 cm long, 2.5 cm wide (high), and 0.3 mm thick.

5.1 Parameter Identification. The same experimental prototype (with a different tail) was used in Ref. [12] to validate a dynamic model for a robotic fish with a rigid tail. The following parameters for the robot were identified in Ref. [12]: $c = 0.07$ m, $m_b = 0.311$ kg, $\rho = 1000$ kg/m^3, $S = 0.0108$ m^2, $J_{bz} = m_b(2c)^2/12$. The added masses and inertias are calculated by approximating the robot body as a prolate spheroid [10,57]: $-X_{\dot{V}_{Cx}} = 0.0621$ kg, $-Y_{\dot{V}_{Cy}} = 0.2299$ kg, and $-N_{\dot{\omega}_z} = 1.0413 \times 10^{-4}$ kg $\cdot$ m^2.

The drag and lift coefficients, C_D, C_L, and C_M, are also identified empirically for the robotic fish with a rigid tail and then used in validating the flexible tail models. In particular, we have tuned

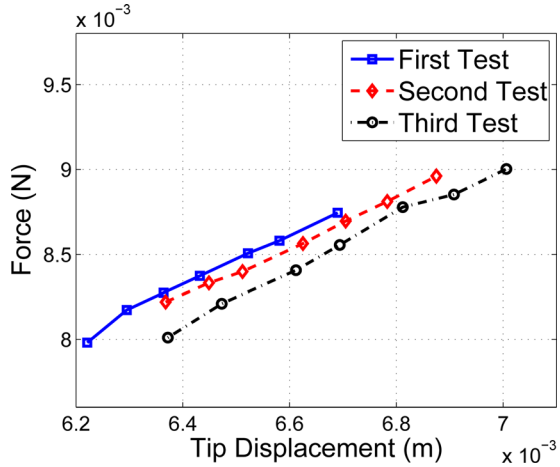

Fig. 7 Experimental results for measuring the Young's modulus of the flexible tail

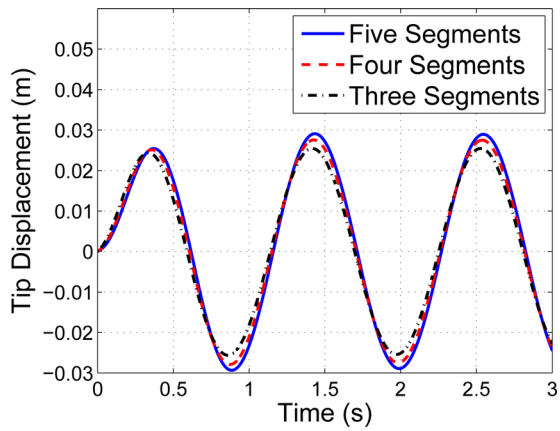

Fig. 8 Displacement of the tail tip generated by the model using different number of rigid segments

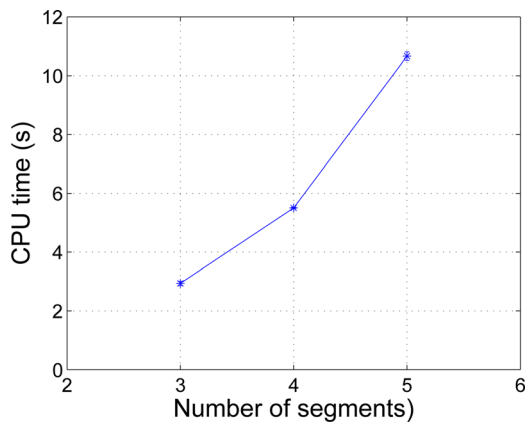

Fig. 9 Computation time needed to simulate the model using different numbers of rigid segments

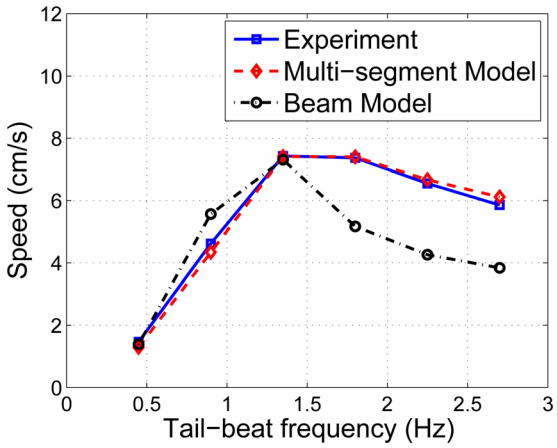

Fig. 10 Comparison between model predictions and experimental measurement of the speed versus tail-beat frequency. The amplitude is fixed at 13.6 deg

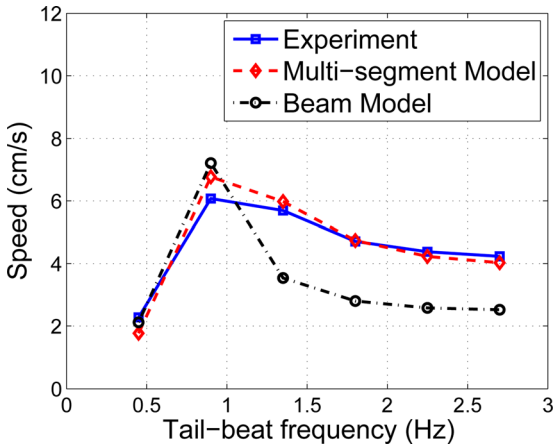

Fig. 11 Comparison between model predictions and experimental measurement of the speed versus tail-beat frequency, with the new tail. The amplitude is fixed at 13.6 deg

these parameters to match the turning radius, turning period, and the average of $|\beta|$ obtained in simulation, with the experimental measurements recorded for a particular tail beat pattern. We set amplitude $\alpha_A = 13.6$ deg, frequency $\omega_\alpha = 1.8\pi$ rad/s (0.9 Hz) and evaluate the suitable drag and lift coefficients for the tail-beat bias α_0 equal to 20 deg, 30 deg, and 40 deg as Ref. [13]. Using least-square-error fitting, we obtain $C_D = 0.276$, $C_L = 4.5$, and $C_M = 7.4 \times 10^{-4}\,\text{kg}\cdot\text{m}^2$, when $\alpha_0 = 0$.

For measuring the Young's modulus, we setup the experiment shown in Fig. 6, and evaluate E using

$$E = \frac{L_b^3 P_L}{3 I_b w_L} \tag{50}$$

where L_b and I_b are the length and the area of moment inertia of the testing beam, respectively. P_L is the load at the tip end, and w_L is the end's displacement. A plastic beam (the same material as the flexible tail) is clamped at the upper surface of a rectangular block, which is fixed on a piston that can move up and down along the stand. A custom LabVIEW (2011 SP1) virtual instrument graphical user interface (GUI) is developed to perform the data acquisition through a dSPACE system (RTI 1104, dSPACE). The force exerted on the beam is captured by a load cell (GS-10, Transducer Techniques) with a custom-made amplifier circuit. The displacement of the beam tip is measured with a laser sensor (OADM 20I6441/S14F, Baumer Electric). Prior to experiment, the system is calibrated with a weight applied to the load cell. Three sets of data are collected to calculate the Young's modulus, and in each set, a least square error method is adopted to approximate the slope between the force and displacement. Figure 7 shows results for three tests, indicating that $E \in [1.41, 1.51]$ GPa. In this work, we take the average $E = 1.48$ GPa.

When modeling a tail using the multisegment approximation, the number of rigid segments affects both modeling accuracy and computational complexity [51]. Specifically, a higher number of elements results in a more accurate model, but is also more computation-intensive. Figure 8 shows the simulated responses of the beam tip displacement (relative to the x axis along the body) to a sinusoidal base excitation, when different numbers of segments are used to model the flexible beam. The properties of the beam used in the simulation are same as those of the beam identified from the experiments. It can be observed that, the beam tip displacements gradually converge to each other when the number of segments increases. Figure 9 shows the running time needed for the simulation illustrated in Fig. 8, which was conducted with MATLAB/SIMULINK on a desktop PC (Dell Vostro 460 with 3.1 GHz Intel i5-2400 central processing unit (CPU) and 4 GB memory). In particular, for all cases, the fundamental sampling time in SIMULINK is fixed at 0.000167 s, the simulation time is set to be 10 s in total, and the elapsed CPU time is obtained using the MATLAB macro *cputime*. We can see that the computation time increases rapidly with the number of rigid segments used in the simulation. A five-segment approximation achieves a sound tradeoff between the modeling accuracy and computational efficiency, and therefore is adopted in this study.

According to Eq. (39), we have $K_S = 5.2 \times 10^{-3}$ N·m that is used in the model using multisegment approximation. The values of κ are identified empirically by fitting the data of forward speed versus beating frequency for both models. In particular, we choose the value of κ such that the simulated steady-state speed of the

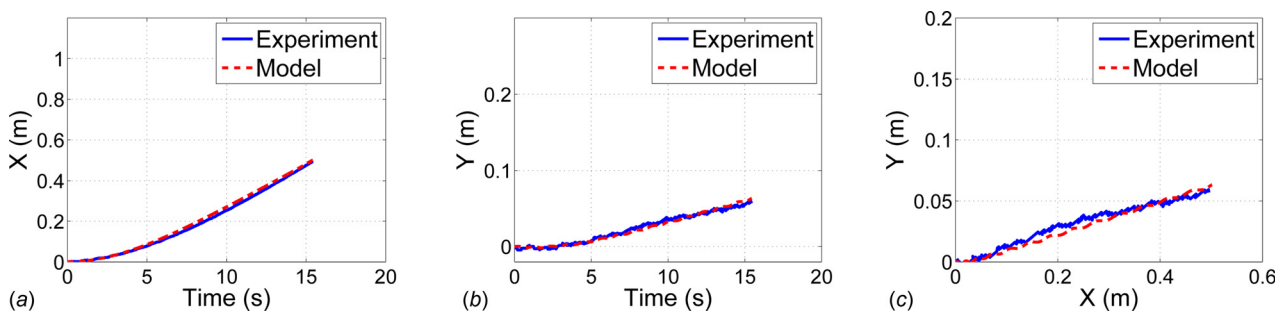

Fig. 12 Comparison between multisegment model predictions and experimental measurement for forward swimming (including transients): (*a*) time trajectory of *X*-coordinate of the robot; (*b*) time trajectory of the *Y*-coordinate of the robot; (*c*) path of the robot in the *XY*-plane. For both the experiment and simulations, the amplitude and frequency of the tail beat are fixed at 13.6 deg and 0.9 Hz, respectively.

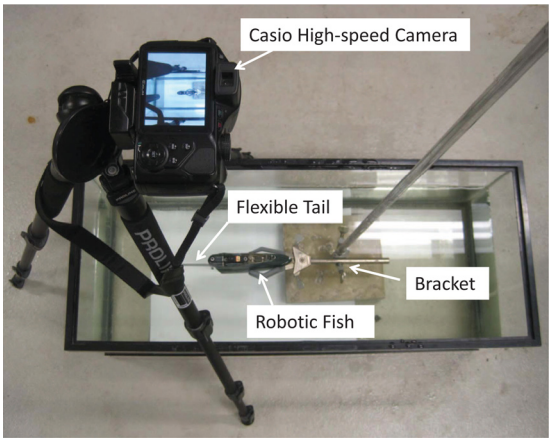

Fig. 13 Experimental setup to capture the dynamic shape of a flexible tail actuated at the base (top view).

robot, when $\alpha_0 = 0$ deg, matches the experimental results when the tail beats at 0.45 Hz, 0.9 Hz, and 1.35 Hz, respectively (for which cases the flexible tail undergoes relatively small deformations). This results in $\kappa = 0.0846$ s for the Euler–Bernoulli beam model and $\kappa = 0.0731$ s for the multisegment approximation model. We take the average $\kappa = 0.079$ s, which leads to $K_D = 4.1 \times 10^{-3}$ N·m·s, using $K_D = \kappa K_S$. These parameters are then applied in the simulation of all other cases.

5.2 Model Verification. Figure 10 compares the two models and experimental measurements in terms of the steady-state speed of the robotic fish with respect to the actuation frequency. The trends are similar for the two model predictions. In particular, the robot's speed increases with the frequency up to a threshold value (1.35 Hz in the simulated case) and then starts to drop. While the predictions from both models match the experiments relatively well (due to the tuning process for parameter κ as described in the previous subsection 5.1), the discrepancy between the predictions becomes larger as the actuation frequency increases. The flexible tail is subjected to the added mass effect as explained in Eq. (11). Under a high-frequency excitation, the lateral hydrodynamic loading on the tail increases and causes larger deformation of the tail. By using linear Euler–Bernoulli beam theory, we assume that the tail is under small deformation, and thus the motion direction of each point along the flexible tail is perpendicular to the dashed line in Fig. 3. The latter assumption no longer holds when the excitation frequency gets high due to the large deformation, which explains the poor prediction performance of the linear beam model at relatively high frequencies. On the other hand, the model using the multisegment approximation matches the experimental measurement closely throughout the actuation frequency range used in the experiments.

To further compare the two models under different conditions, a second experiment has been conducted with another tail of different dimensions, which is 2.34 cm high and 9.8 cm long. Following Eq. (39) and the linear relationship $K_D = \kappa K_S$, the values of K_S and K_D are updated from the original $K_S = 5.2 \times 10^{-3}$ N·m and $K_D = 4.1 \times 10^{-3}$ N·m·s to $K_S = 4.0 \times 10^{-3}$ N·m and $K_D = 3.13 \times 10^{-3}$ N·m·s, respectively. Figure 11 shows the comparison between the two models and the experimental measurements for the robot with the new tail. Consistent with the results in Fig. 10, one can see that the model using the multisegment approximation matches the experimental measurement closely for all actuation frequencies, while the linear beam model performs well only for low-frequency actuation.

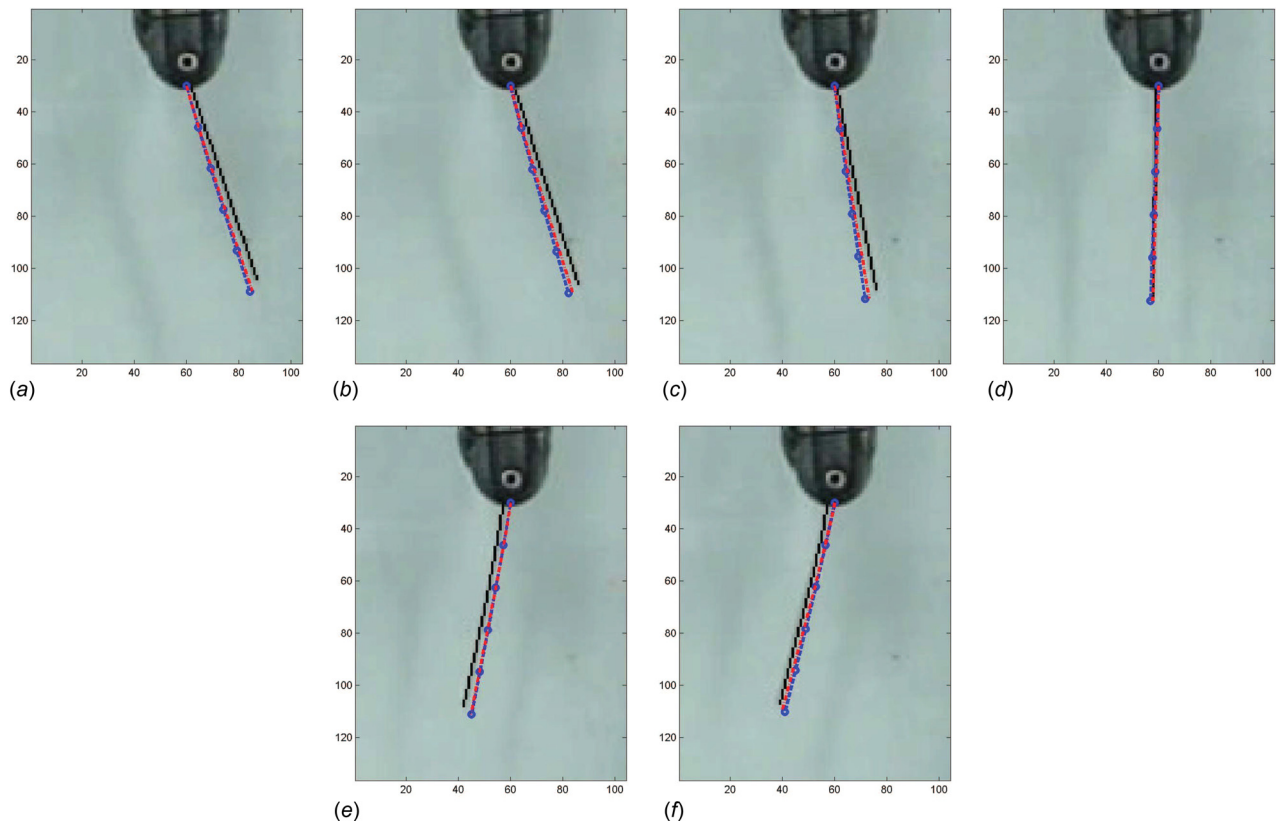

Fig. 14 Comparison between experimental measurement of the time-dependent tail shape with model predictions. The tail beats at 0.4 Hz with 0 deg bias and 14 deg amplitude. The black solid line, blue dashed line with circles and the red dashed-dotted line imply the experimental measurement, predictions from multisegment model and Euler–Bernoulli beam model, respectively.

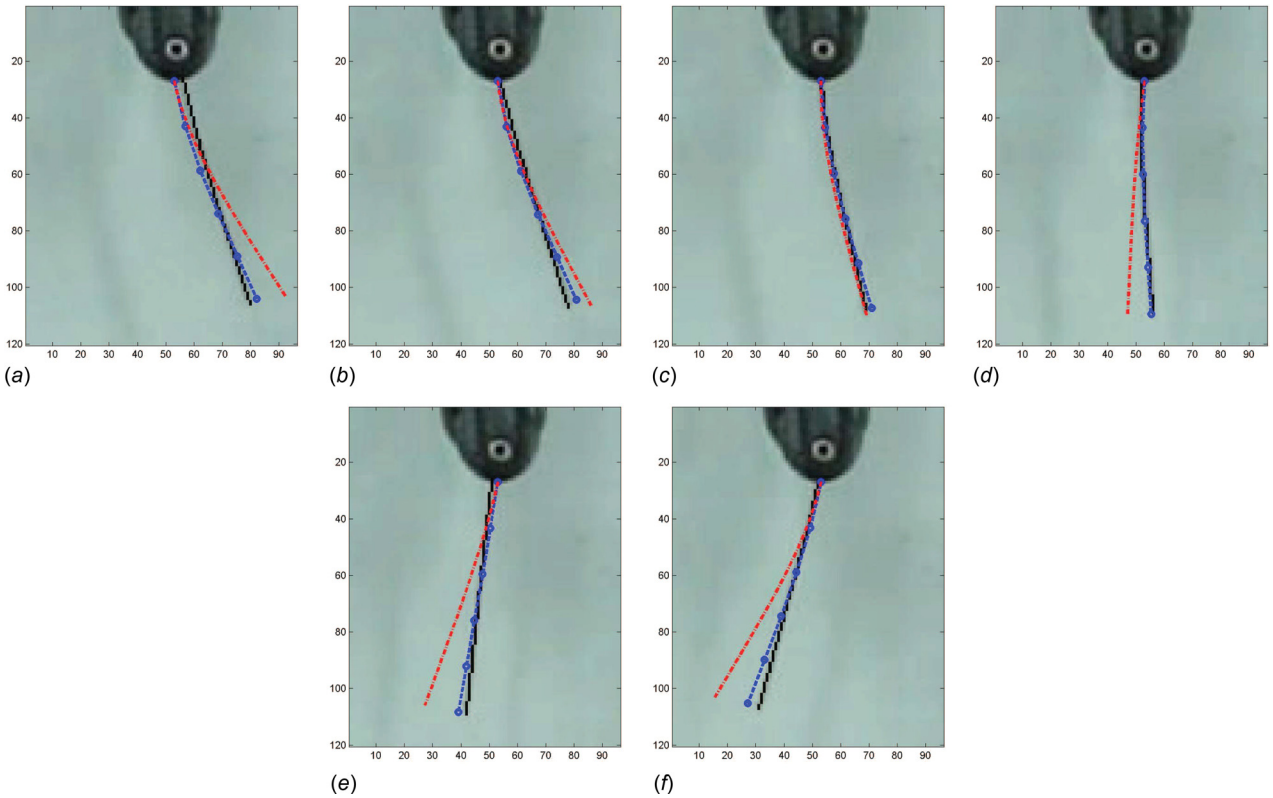

Fig. 15 Comparison between experimental measurement of the time-dependent tail shape with model predictions. The tail beats at 0.9 Hz with 0 deg bias and 13.6 deg amplitude. The black solid line, blue dashed line with circles, and the red dashed-dotted line imply the experimental measurement, predictions from multisegment model and Euler–Bernoulli beam model, respectively.

To further assess the proposed multisegment model, we conduct an experiment involving transients in forward motion, where the robot started from at rest. Figures 12(*a*) and 12(*b*) compare the model predictions of the *X*/*Y*-coordinate time-trajectories of the robot with the experimental measurements, and Fig. 12(*c*) compares the predicted and actual robot paths in the *XY*-plane. It can be seen that the proposed model is able to capture well both the transient and steady-state behaviors of the robot.

We have conducted additional experiments to compare the time-dependent shape of the flexible tail with those predicted by the models. As can be seen in Fig. 13, the free swimming robot shown in Fig. 5 is fixed by a bracket and set to oscillate the tail. A Casio Exilim EX-FH25 high-speed camera with a frame rate of 120 frames/s is used to record the tail's motion from above.

Figures 14 and 15 compare the measured time-dependent tail shape and those predicted by the two models for 0.4 Hz and 0.9 Hz, respectively. To save space, we show every ninth frame for half a period of the tail oscillation. It can be seen that when the tail beats at the relative low-frequency, 0.4 Hz, both models produce very close approximations of the tail shape. However, at 0.9 Hz, when the beam deformation is bigger, the multisegment modeling approach produces much more precise predictions of the beam shape than the linear beam theory-based approach.

6 Conclusion

In this study, we have developed a model for robotic fish with a base-actuated flexible tail. The tail is modeled as multiple rigid segments connected by springs and dampers, and Lighthill's elongated-body theory is used to evaluate the tail-generated hydrodynamic forces. For comparison, we have also constructed a model using linear beam theory. We compare predictions of both models to experimental results with a robotic fish, in terms of steady-state cruising speeds and dynamic tail shapes under different actuation frequencies. From these results, we conclude that when the tail is excited under a relatively low-frequency, and consequently experiences small deformation, both models produce similar predictions that are close to experimental measurements. However, when the actuation frequency increases, the two models differ, and the model using multisegment approximation is able to predict much better the robot speed and the tail shape. Additional experimental results also indicate that the proposed model is capable of capturing the transient dynamics of the robot.

In summary, the work presented in this paper provides a computationally efficient and accurate model for capturing large tail deformation and the resulting hydrodynamic force for a tail-actuated robotic fish. The model will facilitate effective tail design optimization and controller development for such robots. While one could also use nonlinear beam models and CFD to achieve faithful modeling of the tail, the latter approach would be much more computationally expensive, and would be difficult to integrate with the robot dynamics for controller design.

This work can be extended in several directions. First, although this paper has focused on the case of a rectangular tail for ease of presentation, the mathematical derivation itself is general and the approach can be extended to tails of other shapes (e.g., trapezoidal) following a similar treatment, where the properties of each segment (mass, inertia) and each joint (spring and damper constants) will depend on the local shape. Second, we are particularly interested in using the proposed model to understand the effect of tail shape and stiffness properties on the robot's locomotion performance, and exploit such understanding for design optimization. Finally, we will utilize

the proposed model to design controllers for flexible tail-actuated robotic fish.

Acknowledgment

This work has been supported in part by NSF Grant (Nos. CNS-0751155, CCF-0820220, DBI-0939454, IIS-0916720, CNS-0915855, ECCS-1050236, ECCS-1029683, CNS-1059373, CCF-1331852, and IIS-1319602). The authors would like to thank Professor Songlin Chen and Tony Clark for their constructive discussions in this work.

References

[1] Lauder, G. V., and Drucker, E. G., 2004, "Morphology and Experimental Hydrodynamics of Fish Fin Control Surfaces," IEEE J. Oceanic Eng., **29**(3), pp. 556–571.
[2] Fish, F. E., and Lauder, G. V., 2006, "Passive and Active Flow Control by Swimming Fishes and Mammals," Annu. Rev. Fluid Mech., **38**, pp. 193–224.
[3] Triantafyllou, M. S., and Triantafyllou, G. S., 1995, "An Efficient Swimming Machine," Sci. Am., **273**(3), pp. 64–70.
[4] Guo, S., Fukuda, T., and Asaka, K., 2003, "A New Type of Fish-Like Underwater Microrobot," IEEE/ASME Trans. Mechatron., **8**(1), pp. 136–141.
[5] Epstein, M., Colgate, J. E., and MacIver, M. A., 2006, "Generating Thrust With a Biologically-Inspired Robotic Ribbon Fin," Proceedings of the 2006 IEEE/RSJ International Conference on Intelligent Robots and Systems, Oct 9–15, Beijing, China, pp. 2412–2417.
[6] Hu, H., Liu, J., Dukes, I., and Francis, G., 2006, "Design of 3D Swim Patterns for Autonomous Robotic Fish," Proceedings of the 2006 IEEE/RSJ International Conference on Intelligent Robots and Systems, Oct 9–15, Beijing, China, pp. 2406–2411.
[7] Kim, B., Kim, D., Jung, J., and Park, J., 2005, "A Biomimetic Undulatory Tadpole Robot Using Ionic Polymer–Metal Composite Actuators," Smart Mater. Struct., **14**, pp. 1579–1585.
[8] Tan, X., Kim, D., Usher, N., Laboy, D., Jackson, J., Kapetanovic, A., Rapai, J., Sabadus, B., and Zhou, X., 2006, "An Autonomous Robotic Fish for Mobile Sensing," Proceedings of the IEEE/RSJ International Conference on Intelligent Robots and Systems, Oct 9–15, Beijing, China, pp. 5424–5429.
[9] Morgansen, K. A., Triplett, B. I., and Klein, D. J., 2007, "Geometric Methods for Modeling and Control of Free-Swimming Fin-Actuated Underwater Vehicles," IEEE Trans. Rob., **23**(6), pp. 1184–1199.
[10] Aureli, M., Kopman, V., and Porfiri, M., 2010, "Free-Locomotion of Underwater Vehicles Actuated by Ionic Polymer Metal Composites," IEEE/ASME Trans. Mechatron., **15**(4), pp. 603–614.
[11] Low, K. H., 2006, "Locomotion and Depth Control of Robotic Fish With Modular Undulating Fins," Int. J. Autom. Comput., **4**, pp. 348–357.
[12] Wang, J., Alequin-Ramos, F., and Tan, X., 2011, "Dynamic Modeling of Robotic Fish and Its Experimental Validation," Proceedings of the 2011 IEEE/RSJ International Conference on Intelligent Robots and Systems, Sep 25–30, San Francisco, CA pp. 588–594.
[13] Wang, J., and Tan, X., 2013, "A Dynamic Model for Tail-actuated Robotic Fish With Drag Coefficient Adaptation," Mechatronics, **23**(6), pp. 659–668.
[14] Yu, J., Tan, M., Wang, S., and Chen, E., 2004, "Development of a Biomimetic Robotic Fish and its Control Algorithm," IEEE Trans. Syst. Man Cybern. Part B Cybern., **34**(4), pp. 1798–1810.
[15] Zhang, Z. G., Yamashita, N., Gondo, M., Yamamoto, A., and Higuchi, T., 2008, "Electrostatically Actuated Robotic Fish: Design and Control for High-Mobility Open-Loop Swimming," IEEE Trans. Rob., **24**(1), pp. 118–129.
[16] Kanso, E., and Newton, P. K., 2009, "Passive Locomotion via Normal-Mode Coupling in a Submerged Spring-Mass System," J. Fluid Mech., **641**, pp. 205–215.
[17] Alvarado, P. V., and Youcef Toumi, K., 2006, "Design of Machines With Compliant Bodies for Biomimetic Locomotion in Fluid Environments," ASME J. Dyn. Syst. Meas. Control, **128**(1), pp. 3–13.
[18] Wang, Y., Tan, R., Xing, G., Wang, J., and Tan, X., 2012, "Profiling Aquatic Diffusion Process Profiling Using Robotic Sensor Networks," IEEE Trans. Mob. Comput., **13**(4), pp. 883–893.
[19] Wang, Y., Tan, R., Xing, G., Tan, X., Wang, J., and Zhou, R., 2012, "Spatiotemporal Aquatic Field Reconstruction Using Robotic Sensor Swarm," Proceedings of the 33rd IEEE Real-Time Systems Symposium (RTSS), Dec 4–7, San Juan, Puerto Rico, pp. 205–214.
[20] Tan, X., 2011, "Autonomous Robotic Fish as Mobile Sensor Platforms: Challenges and Potential Solutions," Mar. Technol. Soc. J., **45**(4), pp. 31–40.
[21] Marras, S., and Porfiri, M., 2012, "Fish and Robots Swimming Together: Attraction Towards the Robot Demands Biomimetic Locomotion," J. R. Soc. Interface, **9**(73), pp. 1856–1868.
[22] Kato, N., 2000, "Control Performance in the Horizontal Plane of a Fish Robot with Mechanical Pectoral Fins," IEEE J. Oceanic Eng., **25**(1), pp. 121–129.
[23] Anderson, J. M., and Chhabra, N. K., 2002, "Maneuvering and Stability Performance of a Robotic Tuna," Integr. Comp. Biol., **42**, pp. 118–126.
[24] Bandyopadhyay, P. R., 2002, "Maneuvering Hydrodynamics of Fish and Small Underwater Vehicles," Integr. Comp. Biol., **42**, pp. 102–117.
[25] Long, J. H., Lammert, A. C., Pell, C. A., Kemp, M., Strother, J. A., Crenshaw, H. C., and McHenry, M. J., 2004, "A Navigational Primitive: Biorobotic Implementation of Cycloptic Helical Klinotaxis in Planar Motion," IEEE J. Oceanic Eng., **29**(3), pp. 795–806.
[26] Liu, J., and Hu, H., 2010, "Biological Inspiration: From Carangiform Fish to Multi-Joint Robotic Fish," J. Bionic Eng., **7**(1), pp. 35–48.
[27] Krieg, M., and Mohseni, K., "Dynamic Modeling and Control of Biologically Inspired Vortex Ring Thrusters for Underwater Robot Locomotion," IEEE Trans. Rob., pp. 542–554.
[28] Kodati, P., Hinkle, J., Winn, A., and Deng, X., 2008, "Microautonomous Robotic Ostraciiform (MARCO): Hydrodynamics, Design, and Fabrication," IEEE Trans. Rob., **24**(1), pp. 105–117.
[29] Low, K. H., and Chong, C. W., 2010, "Parametric Study of the Swimming Performance of a Fish Robot Propelled by a Flexible Caudal Fin," Bioinspiration Biomimetics, **5**(4), p. 046002.
[30] Chen, Z., Shatara, S., and Tan, X., 2010, "Modeling of Biomimetic Robotic Fish Propelled by an Ionic Polymer-Metal Composite Caudal Fin," IEEE/ASME Trans. Mechatron., **15**(3), pp. 448–459.
[31] Yu, J., Ding, R., Yang, Q., Tan, M., Wang, W., and Zhang, J., 2011, "On a Bio-Inspired Amphibious Robot Capable of Multimodal Motion," IEEE/ASME Trans. Mechatron., **17**(5), pp. 1–10.
[32] Liu, F., Lee, K.-M., and Yang, C.-J., 2012, "Hydrodynamics of an Undulating Fin for a Wave-Like Locomotion System Design," IEEE/ASME Trans. Mechatron., **17**(3), pp. 554–562.
[33] Zhou, C., and Low, K. H., 2012, "Design and Locomotion Control of a Biomimetic Underwater Vehicle With Fin Propulsion," IEEE/ASME Trans. Mechatron., **17**(1), pp. 25–35.
[34] Lee, S., Park, J., and Han, C., 2007, "Optimal Control of a Mackerel-Mimicking Robot for Energy Efficient Trajectory Tracking," J. Bionic Eng., **4**(4), pp. 209–215.
[35] Barrett, D. S., Triantafyllou, M. S., Yue, D. K. P., Grosenbaugh, M. A., and Wolfgang, M. J., 1999, "Drag-Reduction in Fish-Like Locomotion," J. Fluid Mech., **392**, pp. 183–212.
[36] Low, K. H., Chong, C. W., and Zhou, C., 2010, "Performance Study of a Fish Robot Propelled by a Flexible Caudal Fin," Proceedings of the 2010 IEEE International Conference on Robotics and Automation, May 3–8, Anchorage, AK pp. 90–95.
[37] Mason, R., and Burdick, J. W., 2000, "Experiments in Carangiform Robotic Fish Locomotion," Proceedings of the 2000 IEEE International Conference on Robotics and Automation, Apr 24–28, San Francisco, CA, pp. 428–435.
[38] Long, J. H., Jr., Koob, T. J., Irving, K., Combie, K., Engel, V., Livingston, H., Lammert, A., and Schumacher, J., 2006, "Biomimetic Evolutionary Analysis: Testing the Adaptive Value of Vertebrate Tail Stiffness in Autonomous Swimming Robots," J. Exp. Biol., **209**(23), pp. 4732–4746.
[39] Tangorra, J. L., Lauder, G. V., Hunter, I. W., Mittal, R., Madden, P. G. A., and Bozkurttas, M., 2010, "The Effect of Fin Ray Flexural Rigidity on the Propulsive Forces Generated by a Biorobotic Fish Pectoral Fin," J. Exp. Biol., **213**, pp. 4043–4054.
[40] Park, Y., Jeong, U., Lee, J., Kwon, S., Kim, H., and Cho, K., 2012, "Kinematic Condition for Maximizing the Thrust of a Robotic Fish Using a Compliant Caudal Fin," IEEE Trans. Rob., **28**(6), pp. 1216–1227.
[41] Kane, T. R., Ryan, R., and Banerjee, A. K., 1987, "Dynamics of a Cantilever Beam Attached to a Moving Base," J. Guid. Control Dyn., **10**(2), pp. 139–151.
[42] Mitchell, T. P., and Bruch, J. C., 1988, "Free Vibrations of a Flexible Arm Attached to a Compliant Finite Hub," ASME J. Vib. Acoust., **1**(1), pp. 118–120.
[43] Low, K. H., 1990, "Eigen-Analysis of a Tip-Loaded Beam Attached to a Rotating Joint," ASME J. Vib. Acoust., **112**(4), pp. 497–500.
[44] Kelly, S. D., and Murray, R. M., 2000, "Modelling Efficient Pisciform Swimming for Control," Int. J. Robust Nonlinear Control, **10**, pp. 217–241.
[45] Harper, K. A., Berkemeier, M. D., and Grace, S., 1998, "Modeling the Dynamics of Spring-Driven Oscillating-Foil Propulsion," IEEE J. Oceanic Eng., **23**(3), pp. 285–296.
[46] Kopman, V., and Porfiri, M., 2013, "Design, Modeling, and Characterization of a Miniature Robotic Fish for Research and Education in Biomimetics and Bioinspiration," IEEE Trans. Mechatron., **18**(2), pp. 471–483.
[47] Yang, H., Hong, J., and Yu, Z., 2003, "Dynamics Modelling of a Flexible Hub-Beam System With a Tip Mass," J. Sound Vib., **266**(4), pp. 759–774.
[48] Shi, P., McPhee, J., and Heppler, G. R., 2001, "A Deformation Field for Euler-Bernoulli Beams With Applications to Flexible Multibody Dynamics," Multibody Sys. Dyn., **5**(1), pp. 79–104.
[49] Banerjee, A. K., and Nagarajan, S., 1997, "Efficient Simulation of Large Overall Motion of Beams Undergoing Large Deflection," Multibody Sys. Dyn., **1**(1), pp. 113–126.
[50] Wereley, N., Wang, G., and Chaudhuri, A., 2011, "Demonstration of Uniform Cantileverd Beam Beding Vibration Using a Pair of Piezoelectric Actuators," J. Intell. Mater. Syst. Struct., **22**(4), pp. 307–316.
[51] Chen, X., Zhu, G., Yang, X., Hung, D. L. S., and Tan, X., 2013, "Model-Based Estimation of Flow Characteristics Using an Ionic Polymer-Metal Composite Beam," IEEE/ASME Trans. Mechatron., **18**(3), pp. 932–943.
[52] Lighthill, M. J., 1971, "Large-Amplitude Elongated-Body Theory of Fish Locomotion," Proc. R. Soc. London, Ser. B, **179**, pp. 125–138.

[53] Pedley, T. J., and Hill, S. J., 1999, "Large-amplitude Undulatory Fish Swimming: Fluid Mechanics Coupled to Internal Mechanics," J. Exp. Biol., **202**, pp. 3431–3438.
[54] Cheng, J., Zhuang, L., and Tong, B., 1991, "Analysis of Swimming Three-Dimensional Waving Plates," J. Fluid Mech., **232**, pp. 341–355.
[55] Wang, J., McKinley, P. K., and Tan, X., 2012, "Dynamic Modeling of Robotic Fish With a Flexible Caudal Fin," Proceedings of the ASME 2012 5th Annual Dynamic Systems and Control Conference joint with the JSME 2012 11th Motion and Vibration Conference, Oct 17–19, Fort Lauderdale, FL, Paper No. DSCC2012–MOVIC2012–8695.
[56] Fossen, T. I., 1994, *Guidance and Control of Ocean Vehicles*, Wiley, New York.
[57] Arafat, H. N., Stilwell, D. J., and Neu, W. L., 2006, "Development of a Dynamic Model of a Small High-Speed Autonomous Underwater Vehicle," Proceedings of Oceans, Sep 18–22, Boston, MA pp. 1–6.
[58] Clough, R. W., and Penzien, J., 2003, *Dynamics of Structures*, 3rd ed., Computers & Structures Inc, 1995 University Ave, Berkeley, CA.